

## 섬유상 바이러스를 이용한 니켈 수산화물 나노플레이트 제조 및 전기화학 의사커패시터 특성

Manoj Mayaji Ovhal<sup>1</sup> · Hock Beng Lee<sup>2</sup> · Neetesh Kumar<sup>3</sup> · 오진우\*<sup>4</sup> · 강재욱<sup>1</sup>

전북대학교 유연인쇄전자공학과, \*부산대학교 나노에너지공학과  
(2023년 12월 18일 접수, 2024년 1월 9일 수정, 2024년 1월 9일 채택)

## Filamentous Virus-Templated Nickel Hydroxide Nanoplates as Novel Electrochemical Pseudocapacitor Materials

Manoj Mayaji Ovhal<sup>1</sup>, Hock Beng Lee<sup>2</sup>, Neetesh Kumar<sup>3</sup>, Jin-Woo Oh\*<sup>4</sup>, and Jae-Wook Kang<sup>1</sup>

Department of Flexible and Printable Electronics, LANL-JBNU Engineering Institute-Korea,  
Jeonbuk National University, Jeonju 54896, Korea

\*Department of Nano Fusion Technology, Department of Nanoenergy Engineering,  
Research Center for Energy Convergence and Technology, Pusan National University, Busan 46241, Korea

(Received December 18, 2023; Revised January 9, 2024; Accepted January 9, 2024)

**초록:** 본 연구는 M13 박테리오파지라는 생물학적 템플릿 위에 니켈 수산화물(Ni(OH)<sub>2</sub>) 나노구조체를 *in-situ* 성장시켜 섬유 모양의 뛰어난 전기화학적 특성을 가지는 M13-Ni(OH)<sub>2</sub> 전극을 개발하였다. 개발된 M13-Ni(OH)<sub>2</sub> 전극의 면적당 전기용량(C<sub>a</sub>)은 14 mF/cm<sup>2</sup>로 기존의 Ni(OH)<sub>2</sub> 전극(C<sub>a</sub>~18 mF/cm<sup>2</sup>) 보다 28% 증가된 우수한 특성을 보였다. 이러한 향상된 전기화학적 성능은 표면 거칠기 증가, 충전/방전 사이트 향상 및 전하 전달 저항 감소에 기인하였으며, 또한 기존 Ni(OH)<sub>2</sub> 전극 대비 18% 향상된 cycle 안정성을 보였다. 이 연구는 에너지 저장 분야에서 새로운 금속 산화물 나노구조체의 성장을 제어하기 위한 생체 템플릿의 사용 가능성을 보여주었다.

**Abstract:** Pseudocapacitive metal hydroxide nanostructures are promising active electrode materials for supercapacitor applications. Here, we demonstrate the *in-situ* growth of nickel hydroxide (Ni(OH)<sub>2</sub>) nanostructures on filamentous M13 bacteriophage template. The M13-Ni(OH)<sub>2</sub> bio-nanostructure exhibits a fibrous morphology and a preferential growth orientation along the (001) crystal plane. Interestingly, the M13-Ni(OH)<sub>2</sub> electrode demonstrates superior electrochemical properties. The areal capacitance (C<sub>a</sub>) of M13-Ni(OH)<sub>2</sub> and Ni(OH)<sub>2</sub> electrodes was 18 mF/cm<sup>2</sup> and 14 mF/cm<sup>2</sup>, respectively, indicating a 28% increase. The improved electrochemical performance is due to the increased surface roughness, enhanced charge adsorption/desorption sites, and reduced charge transfer resistance. This also contributed to an 18% increase in cyclic stability compared to the Ni(OH)<sub>2</sub> electrode analogue. Overall, this work successfully shows the use of a bio-template to control the growth of novel metal-oxide nanostructures for energy storage applications.

**Keywords:** M13 bacteriophage, active electrode, hydrothermal, energy storage, supercapacitor.

### Introduction

Genetically engineered, filamentous M13 bacteriophage has demonstrated great potential to be used as a green bio-template for the *in-situ* growth of metal hydroxides/oxides and the anchoring of nanostructure metal or metal oxides.<sup>1-3</sup> In general, a single strand 6.6 nm in width and 880 nm in length M13 bacteriophage comprises 2700 copies of the helically arranged pVII

proteins on the phage body, and more copies of pIII, pVI, and pIX proteins or more are located at each end of the bacteriophage. These peptide receptors on M13 bacteriophage are negatively charged, which is favorable to attracting positively charged metal ions to grow functional materials with nanofibrous structures.<sup>3</sup> The peptide receptors of the M13 bacteriophage are closely spaced and can be genetically and chemically modified to form specific shapes with designated functions. Therefore, M13 bacteriophage can be used as a template to determine the homogeneous distribution and percolated network structures of organic/inorganic nanostructures under ambient conditions.<sup>4,6</sup> A further tuning of the pH of the solution, additives,

<sup>†</sup>To whom correspondence should be addressed.  
jwkang@jbnu.ac.kr, ORCID<sup>®</sup>0000-0002-1412-6179  
©2024 The Polymer Society of Korea. All rights reserved.

annealing temperature, and duration during the hydrothermal process can produce hybrid nanostructures of different morphologies.

Owing to its ubiquitous features, such as highly tunable structural geometry aspect ratio, the use of M13 bacteriophage has become increasingly popular in sensing energy harvesting/storage applications. In some studies, M13 bacteriophage is used as a green bio-template for spontaneous and homogenous anchoring metallic/plasmonic nanoparticles under ambient conditions, creating novel bio-nanostructures with fascinating material properties.<sup>2,4</sup> The incorporation of versatile M13-templated fibrous nanostructures has enabled noticeable improvement in the performance of photovoltaic, optoelectronic, and bio-sensing devices.<sup>4,5,7</sup>

The use of M13 bacteriophage for energy storage devices has been scarcely reported.<sup>4,5,8,9</sup> The nanoplate shape of nickel hydroxide ( $\text{Ni}(\text{OH})_2$ ) shows pseudocapacitive electrochemical behavior.<sup>10</sup> However, the nanoplate shape  $\text{Ni}(\text{OH})_2$  was scattered and disconnected in the pristine state, which can hinder interfacial charge transfer due to the prolonged inter-distance between the two nanoplates. For this work, we utilized M13 bacteriophage as a bio-template to grow and self-assemble  $\text{Ni}(\text{OH})_2$  nanoplates through hydrothermal synthesis. The FESEM result demonstrated that the M13 bacteriophage has ordered assembly of  $\text{Ni}(\text{OH})_2$  nanoplates, which creates and maintains the gaps, resulting in M13- $\text{Ni}(\text{OH})_2$  bio-nanoplates formation. The XRD and FTIR results confirm that no impurity phases are present in the presence of the M13 bacteriophage. Both the scattered  $\text{Ni}(\text{OH})_2$  and assembled M13- $\text{Ni}(\text{OH})_2$  bio-nanoplate samples have preferential growth orientation along the (001) plane. Moreover, the M13- $\text{Ni}(\text{OH})_2$  bio-nanoplates have a higher crystallinity level than the scattered  $\text{Ni}(\text{OH})_2$  nanoplates.

The electrochemical performance of  $\text{Ni}(\text{OH})_2$  nanoplates and M13- $\text{Ni}(\text{OH})_2$  bio-nanoplates was studied by incorporating them as an interfacial enhancer into sandwich-type supercapacitor electrodes. The M13- $\text{Ni}(\text{OH})_2$  and  $\text{Ni}(\text{OH})_2$  electrodes achieved areal capacitances of approximately 18  $\text{mF}/\text{cm}^2$  and 14  $\text{mF}/\text{cm}^2$ , respectively, at a 10  $\mu\text{A}/\text{cm}^2$  current density. Electrochemical characterizations reveal that the increased surface adsorption sites and reduced inter-distance between the nanoplates in the M13- $\text{Ni}(\text{OH})_2$  network are mainly responsible for the improved pseudocapacitive performance and galvanostatic charge/discharge stability of the electrodes.

## Experimental

**Materials.** Nickel sulfate hexahydrate ( $\text{NiSO}_4 \cdot 6\text{H}_2\text{O}$ , 99.9%) and ethylene glycol (EG) were purchased from Sigma Aldrich, Republic of Korea. Wild type M13 bacteriophage was provided by Prof. Jin-Woo Oh and his team. The PH-1000 poly(3,4-ethylene dioxathiophene):polystyrene sulfonate (PEDOT:PSS) solution was obtained from Clevious, Germany. A deionized (DI) water plant was installed in the laboratory and subsequently used for all the experiments.

**Hydrothermal Synthesis of M13- $\text{Ni}(\text{OH})_2$  Bio-nanoplates.** The crucial parameters for achieving optimal nanoplate growth include precise control of the hydrothermal growth process (temperature, pressure, time) and maintaining a specific concentration of Ni ions and M13 bacteriophage. M13 bacteriophage was mass amplified using a typical mass amplification protocol.<sup>2</sup> After amplification, a centrifuge-based washing process was followed to purify and concentrate the M13 bacteriophage solution. The resulting M13 bacteriophage concentration was 5  $\text{mg}/\text{mL}$ . The precursor solution of M13- $\text{Ni}(\text{OH})_2$  nanostructure was prepared by mixing the as-bought 10  $\text{mM}$   $\text{NiSO}_4 \cdot 6\text{H}_2\text{O}$  in 50  $\text{mL}$  of DI water with 100  $\mu\text{L}$  of M13-bacteriophage (5 wt%) solution for 1 hour. Thus, the final concentration of M13 bacteriophage in hydrothermal solution was only 0.01  $\text{mg}/\text{mL}$ . Further, the final M13- $\text{Ni}(\text{OH})_2$  precursor solution was kept in a hydrothermal process at 120  $^\circ\text{C}$  for 6 hours. The resulting solution was washed and centrifuged five times to yield the final powder of M13- $\text{Ni}(\text{OH})_2$  nanoplates. Whereas, only  $\text{Ni}(\text{OH})_2$  nanoplates were synthesized through the same hydrothermal process but without M13.

**Fabrication of Supercapacitor Electrodes.** Supercapacitor composite electrodes were fabricated by sandwiching  $\text{Ni}(\text{OH})_2$  nanoplates or M13- $\text{Ni}(\text{OH})_2$  bio-nanoplates between the top and bottom PEDOT:PSS films. The EG-modified PEDOT:PSS (PEDOT) solution was synthesized by adding 6 vol% of EG into the PEDOT:PSS solution, followed by stirring for 24 h.<sup>11,12</sup> The PEDOT was applied to pre-cleaned glass substrates using a spin-coater at 2000 rpm, after which it was annealed at 150  $^\circ\text{C}$  for 5 min. Next, 2 wt% of  $\text{Ni}(\text{OH})_2$  and M13- $\text{Ni}(\text{OH})_2$  nanoplates in DI water were spin-coated onto the PEDOT electrodes at 1000 rpm, then annealed at 150  $^\circ\text{C}$  for 5 min. Afterwards, PEDOT was again deposited on nanoplates film at 2000 rpm and annealed at 150  $^\circ\text{C}$  for 5 min. The electrochemical performance of these electrodes was then studied.

**Fundamental Characterizations of Supercapacitor Electrodes.** The crystallographic analysis of hydrothermally

synthesized nanoplates was investigated by X-ray diffractometer, XRD (D8 Advanced, Bruker, Germany) with Cu  $K\alpha_1$  source ( $\lambda=1.54 \text{ \AA}$ ). The functional groups in the synthesis nanoplates were studied using Fourier transform infrared spectroscopy FTIR (Frontier, PerkinElmer, USA) measurement. The surface morphologies and topographies of the nanoplates were analyzed through the field-emission scanning electron microscope, FESEM (SUPRA40VP, Carl Zeiss, Germany), and atomic force microscopy, AFM (NX1, Park Systems, Korea), respectively. All the above facilities are provided and maintained by the Center for University-wide Research Facilities (CURF) at Jeonbuk National University.

**Electrochemical Characterizations of Supercapacitor Electrodes.** The electrodes were subjected to electrochemical analysis through the CompactStat (IVIUM Technologies, Netherlands). The three-electrode system opted to evaluate the electrochemical properties of the electrodes with a reference electrode (Ag/AgCl) and counter electrode (platinum wire) in 1M LiCl aqueous electrolyte. The cyclic voltammetry (CV) curves at different scan rates and galvanostatic charge-discharge (GCD) curves at different current densities were recorded. Areal capacitance ( $C_a$ ) was evaluated using GCD curves. The  $C_a$  calculations were conducted using eq. (1), respectively:<sup>11,13</sup>

$$C_a = \frac{n \times I \times \Delta t}{A \times \Delta V} \quad (1)$$

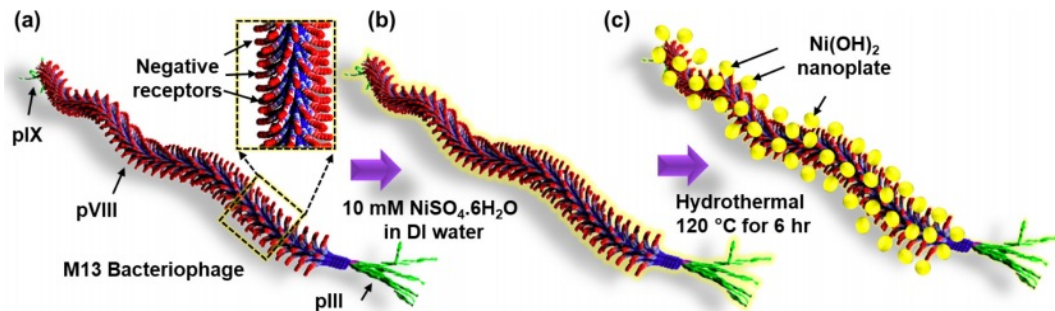


**Figure 1.** Schematic showing *in-situ* growth of  $\text{Ni}(\text{OH})_2$  nanoplates on the M13 bacteriophage: (a) a single strand M13 bacteriophage; (b) Ni ion seeding on M13 bacteriophage; (c) M13- $\text{Ni}(\text{OH})_2$  nanoplates.

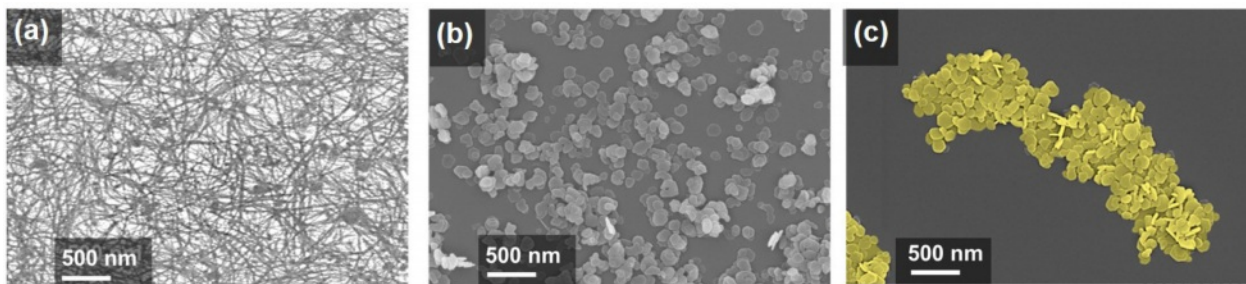


**Figure 2.** Top-view FESEM images of the (a) as-spun M13 bacteriophage network; (b) scattered  $\text{Ni}(\text{OH})_2$  nanoplates; (c) M13- $\text{Ni}(\text{OH})_2$  bio-nanoplates.

In a three-electrode system, the factor  $n$  is a multiple of four,  $A$  represents the area of the electrodes immersed in the electrolyte,  $I$  represents the current density per unit area,  $\Delta t$  represents the discharge time, and  $\Delta V$  represents the voltage difference. The areal energy density ( $E$ ) was determined by eq. (2) and power density ( $P$ ) by eq. (3). The results were presented graphically in the form of Ragone plots.<sup>11,13</sup>

$$E = \frac{1}{2} \times \frac{1}{3600} C_a \times \Delta V^2 \quad (2)$$

$$P = \frac{3600 \times E}{\Delta t} \quad (3)$$

The electrochemical impedance spectroscopy (EIS) measurements were performed and analyzed the EIS parameters such as equivalent series resistance ( $R_s$ ), charge transfer resistance ( $R_c$ ), constant phase element for double-layer capacitance ( $CPE_{DL}$ ), constant phase element for pseudocapacitance ( $CPE_L$ ), and Warburg resistance ( $W_o$ ) using IVIUM software.

## Results and Discussion

### Morphological Properties of M13- $\text{Ni}(\text{OH})_2$ Bio-nanoplates.

Figure 1(a-c) schematically depicts the hydrothermal growth process of M13- $\text{Ni}(\text{OH})_2$  bio-nanoplates, in which M13 bacteriophage functions as a bio-template. Figure 1(a) shows the

schematic of a single strand of M13 bacteriophage with pIII, pVI, and pIX proteins. Figure 1(b) represents the seeding and nucleation of Ni ions on the negative receptors of M13 bacteriophage during the immersion in a nickel sulfate solution. After undergoing a hydrothermal growth process, Ni(OH)<sub>2</sub> nanoplates with uniform shape and size were grown on the M13 bacteriophage in an orderly manner with the remaining gap between them, resulting in the development of M13-Ni(OH)<sub>2</sub> bio-nanoplates (Figure 1(c)) with fascinating structural properties.

High-resolution FESEM images reveal drastically different surface morphologies. Figure 2(a) shows the as-spun M13 bacteriophage network, Figure 2(b) depicts scattered Ni(OH)<sub>2</sub>

nanoplates, and Figure 2(c) shows M13-Ni(OH)<sub>2</sub> bio-nanoplates. The M13 bacteriophage (bio-template) creates an interconnected network of nanoplates with designated gaps. To investigate the crystallinity of the Ni(OH)<sub>2</sub> nanoplates in the presence of M13 bacteriophage, the XRD analysis of powders was performed.<sup>14</sup>

**Structural Properties of M13-Ni(OH)<sub>2</sub> Bio-nanoplates.** The XRD pattern of the scattered Ni(OH)<sub>2</sub> nanoplates and in-situ grown M13-Ni(OH)<sub>2</sub> bio-nanoplates are shown in Figure 3(a). The XRD peaks at 2 $\theta$  positions of 19.03, 32.91, 38.42, 51.87, and 58.94° correspond to (001), (100), (011), (012), and (110) crystal planes, respectively. The XRD patterns of Ni(OH)<sub>2</sub>

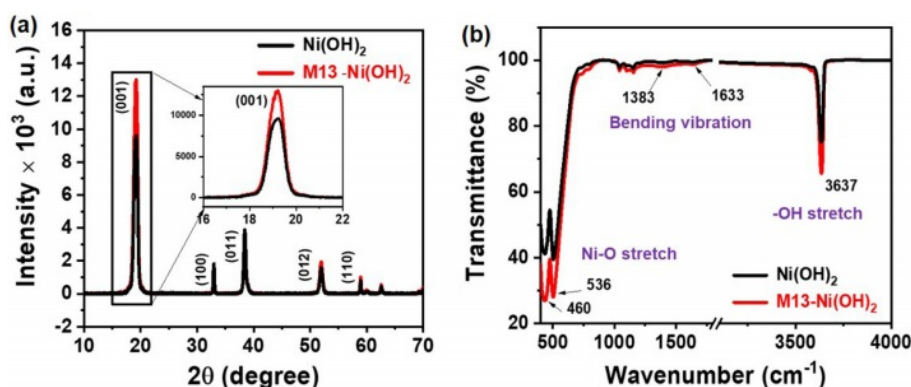


**Figure 3.** Structural characteristics of Ni(OH)<sub>2</sub> nanoplates and M13-Ni(OH)<sub>2</sub> bio-nanoplates: (a) XRD patterns; (b) FTIR spectra.

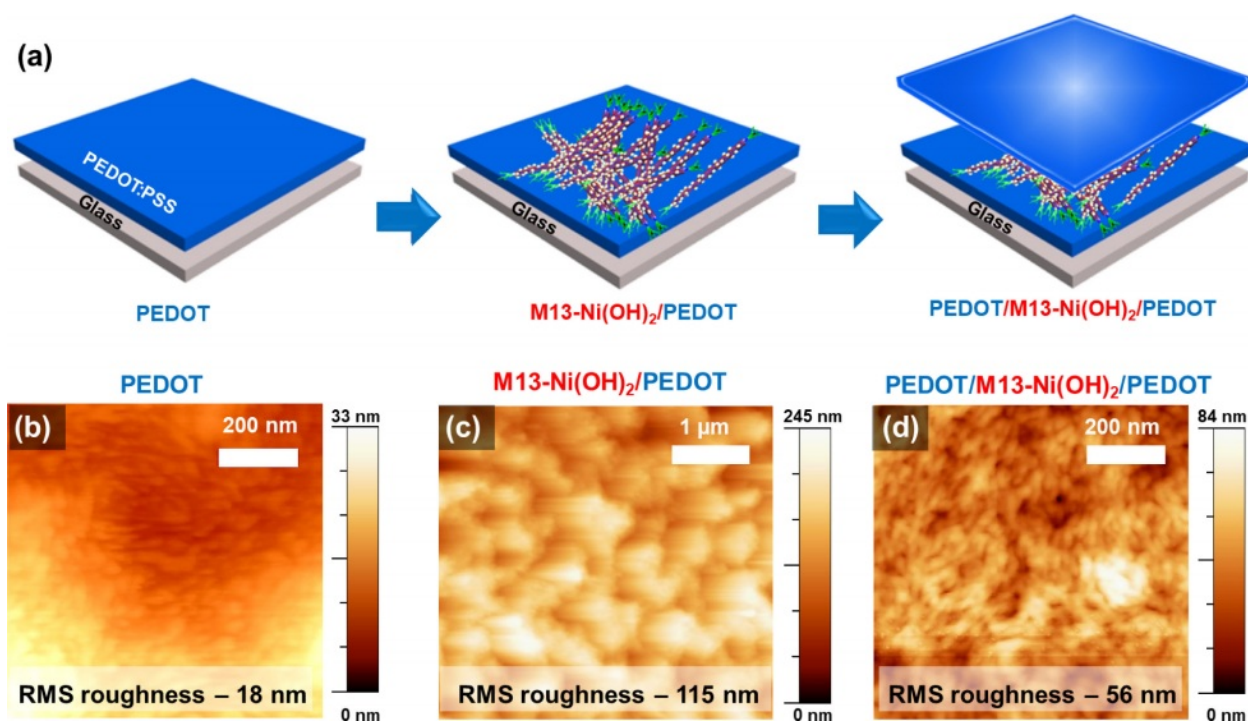


**Figure 4.** (a) Schematic fabrication process of PEDOT/M13-Ni(OH)<sub>2</sub>/PEDOT sandwiched electrodes. AFM micrographs of (b) PEDOT film; (c) M13-Ni(OH)<sub>2</sub>/PEDOT; (d) PEDOT/M13-Ni(OH)<sub>2</sub>/PEDOT electrodes.

nanoplate and M13-Ni(OH)<sub>2</sub> bio-nanoplate were matched well with the reference pattern of JCPDS file no. 70-0989, confirming the  $\beta$ -phase of the two-dimensional Ni(OH)<sub>2</sub> nanoplates.<sup>15,16</sup> The dominant peak at  $2\theta$  positions of 19.03° in Ni(OH)<sub>2</sub> and M13-Ni(OH)<sub>2</sub> pattern confirms the two-dimensional preferential growth of the along (001) crystal plane.<sup>15,17</sup> Interestingly, the intensity of the (001) peak was found to be much higher in the M13-Ni(OH)<sub>2</sub> bio-nanoplate respective to the scattered Ni(OH)<sub>2</sub> nanoplates, representing the superior crystallinity in Ni(OH)<sub>2</sub> nanoplates in the presence of M13 bacteriophage. The XRD result correlates well with the findings in the FESEM images. The directional growth of the Ni(OH)<sub>2</sub> unit cell along the (001) crystal plate is shown in inset Figure 3(a) and schematically in supplementary Figure S1. The results observed in FTIR spectra of Ni(OH)<sub>2</sub> and M13-Ni(OH)<sub>2</sub> nanoplates are presented in Figure 3(b). The prominent peaks were detected at wavenumber of 460 nm<sup>-1</sup> and 536 nm<sup>-1</sup>, confirming the Ni-O functional group in both samples. The peak at 3637 nm<sup>-1</sup> also depicts the O-H stretching observed in both instances, manifesting that the exposed crystal surface was reached in O atoms.<sup>13</sup> The subtle peaks representing O-H bending vibrations were also detected at 1383 and 1633 nm<sup>-1</sup>. The FTIR spectra show no additional peaks due to M13 bacteriophage, evidencing that using M13 bacterio-

phage as a bio-template did not lead to the formation of impurity phases.

Supercapacitor composite electrodes were fabricated by sandwiching scattered Ni(OH)<sub>2</sub> and M13-Ni(OH)<sub>2</sub> bio-nanoplates between the top and bottom PEDOT film electrodes, as illustrated in Figure 4(a). The AFM micrographs show the RMS surface roughness of the pristine M13 bacteriophage on glass (Figure S2), PEDOT electrode (Figure 4(b)), M13-Ni(OH)<sub>2</sub>/PEDOT electrode (Figure 4(c)), and sandwiched electrode (PEDOT/M13-Ni(OH)<sub>2</sub>/PEDOT) (Figure 4(d)) were ~11, ~18, ~115, and ~56 nm, respectively. For ease of elucidation, the sandwiched electrodes with Ni(OH)<sub>2</sub> and M13-Ni(OH)<sub>2</sub> hereafter represented as Ni(OH)<sub>2</sub> electrode and M13-Ni(OH)<sub>2</sub> electrode, respectively, in subsequent discussions.

**Electrochemical Performance of the Electrodes.** Next, the electrochemical performances of the pseudocapacitor Ni(OH)<sub>2</sub> electrode and M13-Ni(OH)<sub>2</sub> electrode were analyzed using CV and GCD. The electrodes were tested under similar conditions to recognize the effect of M13 bacteriophage on their electrochemical performance. Figure 5(a) depicts CV characteristic curves of both electrodes in a voltage range of 0-0.8 V. Its quasi-rectangular shape manifests the ideal pseudocapacitor behavior in both electrodes (Figure S2).<sup>18</sup> Comparatively, the

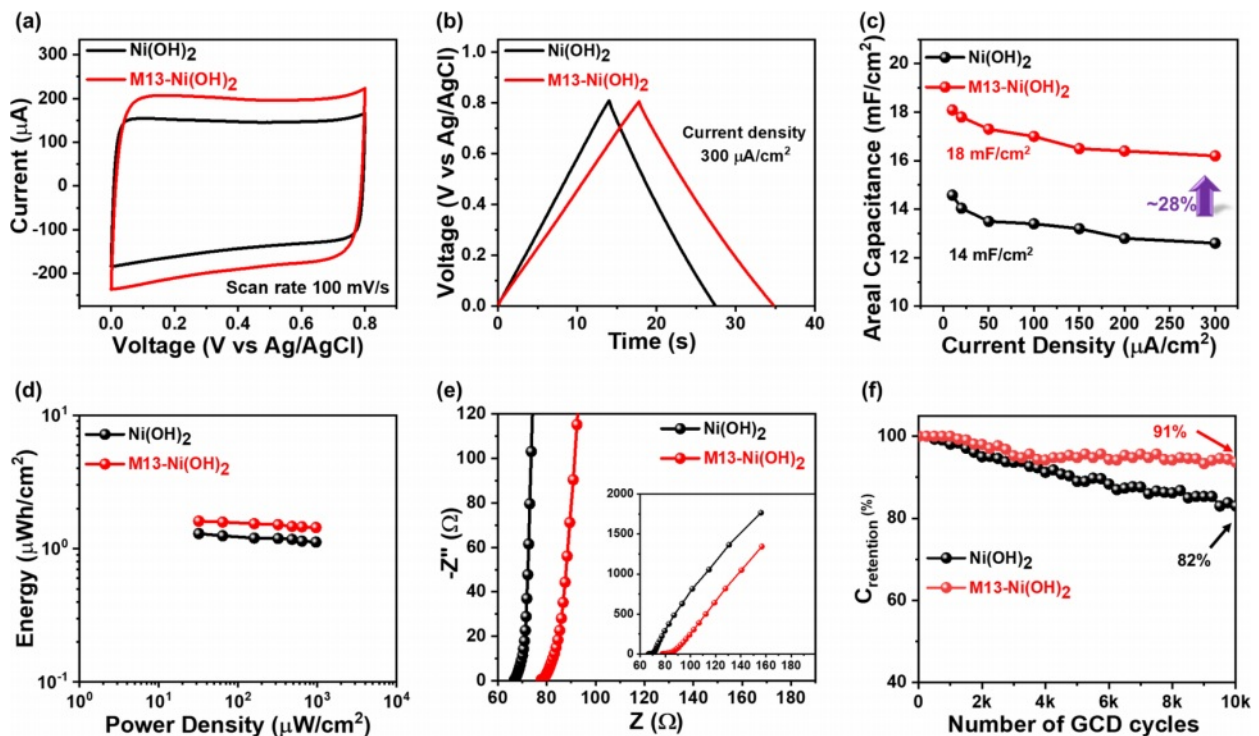


**Figure 5.** Electrochemical properties (measured in three-electrode system) of supercapacitor electrodes: (a) CV; (b) GCD; (c)  $C_a$  vs. applied current density; (d) Ragone plot; (e) Nyquist plot; (f)  $C_{\text{retention}}$  with respective to the 10000 GCD cycles.

M13-Ni(OH)<sub>2</sub> electrode acquires higher current and had a considerably higher CV integral area than analogue, suggesting enhanced electrochemical energy storage capability of the electrodes in the presence of M13 bacteriophage. Similarly, the triangular-shaped GCD profiles (Figure 5(b) and Figure S3) further confirmed fast charge transport and ion diffusion. The charging and discharging time increased to 17 seconds for the M13-Ni(OH)<sub>2</sub> from 13 seconds for the Ni(OH)<sub>2</sub> electrode. The extended time required for charging and discharging indicates that the M13-Ni(OH)<sub>2</sub> electrode can store more charge than analogue. In particular, the charges stored on the surface of the Ni(OH)<sub>2</sub> nanoplate and PEDOT:PSS by electrochemical redox reaction and are shown in eqs. (4) and (5), respectively. The electrochemical reversible redox reaction of Ni(OH)<sub>2</sub> nanoplate in LiCl electrolyte is as follows.<sup>19,20</sup>



Additionally, the improved electrochemical performance was mainly attributed to its mesoporous network-like structure in the presence of M13 bacteriophage, which enhances the electrode surface area, as confirmed by AFM analysis, and is beneficial for ion adsorption.

The areal capacitance ( $C_a$ ) of both electrodes was determined using eq. (1) with GCD current density ranging from 10 to 300  $\mu\text{A}/\text{cm}^2$ , as shown in Figure 5(c). The M13-Ni(OH)<sub>2</sub> electrode achieved a maximum  $C_a$  of around 18  $\text{mF}/\text{cm}^2$ , which was 28% higher compared to its analogue ( $C_a=14 \text{ mF}/\text{cm}^2$ ) even at the same current density (10  $\mu\text{A}/\text{cm}^2$ ). Similarly, the  $E$  was calculated using eq. (2) and  $P$  using eq. (3). The results were presented in Ragone plots in Figure 5(d). The Ni(OH)<sub>2</sub> electrode and M13-Ni(OH)<sub>2</sub> electrode show maximum  $E$  of 1.29  $\mu\text{Wh}/\text{cm}^2$  and 1.62  $\mu\text{Wh}/\text{cm}^2$  at a  $P$  of 32  $\mu\text{W}/\text{cm}^2$ , respectively. The champion electrode developed in this study had a higher  $E$  than its analogue.

In addition, EIS measurements of both electrodes were conducted at the frequency of 1 MHz to 1 Hz. In the Nyquist plots (Figure 5(e)), the electrodes' curves were fitted with a standard equivalent circuit model using IVIUM software. The characteristic EIS parameters values are shown in Table 1.<sup>21</sup> Comparing the  $R_s$  values, the Ni(OH)<sub>2</sub> electrode exhibited  $R_s$  of

$\sim 67.9 \Omega$ , which is significantly lower compared to the M13-Ni(OH)<sub>2</sub>-based electrode ( $R_s \sim 78.1 \Omega$ ). The increase in  $R_s$  may be arising from its M13 bacteriophage, which itself does not contribute to the electrical conductivity or electrochemical charge storage (electric double-layer capacitor and pseudocapacitor) mechanism.<sup>4,9</sup> Meanwhile, there is a substantial difference in the  $R_{ct}$  values of the electrodes based on Ni(OH)<sub>2</sub> ( $R_{ct} \sim 2.77 \Omega$ ) and M13-Ni(OH)<sub>2</sub> ( $R_{ct} \sim 2.18 \Omega$ ), confirming the superior charge transfer of the latter. The  $CPE_{DL}$  values of Ni(OH)<sub>2</sub>- and M13-Ni(OH)<sub>2</sub>-based electrodes were measured to be  $\sim 1.37 \text{ mF}$  and  $\sim 0.47 \text{ mF}$ . Inversely, the  $CPE_L$  values were 1.87  $\text{mF}$  and 2.45  $\text{mF}$ , respectively. A low  $CPE_{DL}$  coupled with a high  $CPE_L$  in the presence of the M13 bacteriophage indicates improved adsorption and intercalation of electrolyte ions and superior capacitance.<sup>21</sup> The significantly higher  $CPE_{DL}$  value of the champion electrode suggests an improved conductivity among the ordered nanoplates.<sup>22</sup>

The  $W_o$  represents the high resistance to diffusion of ions back into the electrolyte, which was observed at lower frequencies to be steeper than 45 degrees in the M13-Ni(OH)<sub>2</sub> electrode compared to analogue.<sup>23,24</sup> This indicates a higher degree of effectiveness in capturing and distributing ions at the interface, making it a promising candidate for various electrochemical applications.<sup>11,19</sup> The study's findings indicate that the scattered nanoplates have restricted ion adsorption, which hinders charge transfer. This limitation is primarily attributed to the nanoplate's low surface-to-volume ratio and disconnected morphology.<sup>20</sup> Meanwhile, the orderly arranged and interconnected nanoplates on the M13 bacteriophage body effectively reduced the distance for ion diffusion. They provided more ion adsorption sites in the electrode, enabling more efficient current collection in the champion electrode. Additionally, the mesoporous morphology of M13-Ni(OH)<sub>2</sub> bio-nanoplates also helped accommodate a significantly higher number of ions at the electrode/electrolyte interface.<sup>25,26</sup>

## Conclusion

This work showcases a new method of producing M13-Ni(OH)<sub>2</sub> bio-nanoplates for supercapacitor devices. The pseudocapacitive Ni(OH)<sub>2</sub> nanoplates were successfully synthesized and grown

**Table 1. EIS Parameters of Ni(OH)<sub>2</sub> Electrode and M13-Ni(OH)<sub>2</sub> Electrodes**

Electrodes	$R_s$ ( $\Omega$ )	$R_{ct}$ ( $\Omega$ )	$CPE_{DL}$ (mF)	$CPE_L$ (mF)	$R_L \times 10^5$ ( $\Omega$ )	$W_o \times 10^{-2}$ ( $\text{S}^{1/2}/\Omega$ )
Ni(OH) <sub>2</sub>	66.9	2.77	1.37	1.87	1.43	6.75
M13-Ni(OH) <sub>2</sub>	78.1	2.18	0.47	2.45	0.13	2.69

onto the M13 bacteriophage using a simple hydrothermal technique. The morphology and structural properties of assembled M13-Ni(OH)<sub>2</sub> bio-nanoplates underwent significant changes. X-ray diffraction analysis revealed that the assembled M13-Ni(OH)<sub>2</sub> exhibited higher crystallinity than the analogue. Furthermore, it was observed that in both cases, the Ni(OH)<sub>2</sub> nanoplates grew preferentially along the (001) oriented plane. Fourier-transform infrared spectroscopy confirmed that the M13 bacteriophage template formed no complex or impurity phases. Furthermore, the hydrothermally synthesis nanoplates were sandwiched between the PEDOT film as an interfacial enhancer. In electrochemical performance, the pseudocapacitor M13-Ni(OH)<sub>2</sub> electrode shows a maximum  $C_a$  of 18 mF/cm<sup>2</sup> superior to its analogue. The primary reason for the increased capacitance is due to the reduced gap between the nanoplates on the M13 bacteriophage, which effectively facilitates charge transfer between the two nanoplates. The M13-Ni(OH)<sub>2</sub> bio-nanoplates also have an improved surface roughness and mesoporous morphology, which enhanced the interfacial area between electrode and electrolyte, providing more ion adsorption sites. Collectively, these changes have led to an 18% improvement in the cyclic stability of the electrodes. M13 bacteriophage as a bio-template for the controlled assembly and *in-situ* growth of metal hydroxide/oxide nanostructures could inspire the development of versatile bio-nanostructures for energy storage applications.

**Acknowledgement:** This work was financially supported by the Basic Science Research Program (NRF-2022R111A1A01070939, 2021R1A2C2004206) and by the Creative Materials Discovery Program (NRF-2017M3D1A1039287) through the National Research Foundation (NRF) of Korea, funded by the Ministry of Science, ICT & Future Planning. This paper was supported by research funds from Jeonbuk National University in 2023.

**Conflict of Interest:** The authors declare that there is no conflict of interest.

**Supporting Information:** Information is available regarding the experimental procedure for AFM micrographs of the pristine M13 bacteriophage and electrochemical properties of Ni(OH)<sub>2</sub> electrode. The materials are available *via* the Internet at <http://journal.polymer-korea.or.kr>.

## References

1. Khalil, A. S.; Ferrer, J. M.; Brau, R. R.; Kottmann, S. T.; Noren,

- C. J.; Lang, M. J.; Belcher, A. M. Single M13 Bacteriophage Tethering and Stretching. *Proc. Natl. Acad. Sci. USA* **2007**, *104*, 4892-4897.
2. Chung, W. J.; Oh, J. W.; Kwak, K.; Lee, B. Y.; Meyer, J.; Wang, E.; Hexemer, A.; Lee, S. W. Biomimetic Self-templating Supramolecular Structures. *Nature* **2011** *478*, 364-368.
3. Mao, C.; Wang, F.; Cao, B. Controlling Nanostructures of Mesoporous Silica Fibers by Supramolecular Assembly of Genetically Modifiable Bacteriophages. *Angew. Chem.* **2012**, *124*, 6517-6521.
4. Moon, J.-S.; Kim, W.-G.; Kim, C.; Park, G.-T.; Heo, J.; Yoo, S. Y.; Oh, J.-W. M13 Bacteriophage-Based Self-Assembly Structures and Their Functional Capabilities. *Mini Rev. Org. Chem.* **2015**, *12*, 271-281.
5. Seo, Y.; Manivannan, S.; Kang, I.; Lee, S. W.; Kim, K. Gold Dendrites Co-deposited with M13 Virus as a Biosensor Platform for Nitrite Ions. *Biosens. Bioelectron.* **2017**, *94*, 87-93.
6. Arter, J. A.; Taggart, D. K.; McIntire, T. M.; Penner, R. M.; Weiss, G. A. Virus-PEDOT Nanowires for Biosensing. *Nano. Lett.* **2010**, *10*, 4858-4862.
7. Lee, B.; Ko, Y.; Kwon, G.; Lee, S.; Ku, K.; Kim, J.; Kang, K. Exploiting Biological Systems: Toward Eco-Friendly and High-Efficiency Rechargeable Batteries. *Joule* **2018**, *2*, 61-75.
8. Lee, H. B.; Kim, W. G.; Lee, M.; Lee, J. M.; He, S.; Kumar, N.; Devaraj, V.; Choi, E. J.; Jeon, I.; Song, M.; Oh, J.-W. Gap Plasmon of Virus-Templated Biohybrid Nanostructures Uplifting the Performance of Organic Optoelectronic Devices. *Adv. Opt. Mater.* **2020**, *8*, 1-8.
9. Nam, K. T.; Kim, D.; Yoo, P. J.; Chiang, C.-Y.; Meethong, N.; Hammond, P. T.; Chiang, Y.; Belcher, A. M. Virus-Enabled Synthesis and Assembly of Nanowires for Lithium Ion Battery Electrodes. *Science* **2006**, *312*, 885-888.
10. Parveen, N.; Cho, M. H. Self-assembled 3D Flower-like Nickel Hydroxide Nanostructures and Their Supercapacitor Applications. *Sci. Rep.* **2016**, *6*, 2-11.
11. Ginting, R. T.; Ovhal, M. M.; Kang, J.-W. A Novel Design of Hybrid Transparent Electrodes for High Performance and Ultra-Flexible Bifunctional Electrochromic-Supercapacitors. *Nano Energy* **2018**, *53*, 650-657.
12. Ouyang, J.; Xu, Q.; Chu, C. W.; Yang, Y.; Li, G.; Shinar, J. On the Mechanism of Conductivity Enhancement in Poly(3,4-ethylenedioxythiophene):poly(styrene sulfonate) Film Through Solvent Treatment. *Polymer (Guildf)* **2004**, *45*, 8443-8450.
13. Zhao, W.; Jiang, M.; Wang, W.; Liu, S.; Huang, W.; Zhao, Q. Flexible Transparent Supercapacitors: Materials and Devices. *Adv. Funct. Mater.* **2021**, *31*, 2009136.
14. Li, T.; Dang, N.; Zhang, W.; Liang, W.; Yang, F. Determining the Degree of [001] Preferred Growth of Ni(OH)<sub>2</sub> Nanoplates. *Nanomaterials* **2018**, *8*, 1-8.
15. Ede, S. R.; Anantharaj, S.; Kumaran, K. T.; Mishra, S.; Kundu, S. One-step Synthesis of Ni/Ni(OH)<sub>2</sub> Nanosheets (NSs) and Their Application in Asymmetric Supercapacitors. *RSC Adv.* **2017**, *7*, 5898-5911.
16. Singu, B. S.; Male, U.; Hong, S. E.; Yoon, K. R. Synthesis and Performance of Nickel Hydroxide Nanodiscs for Redox

- Supercapacitors. *Ionics (Kiel)* **2016**, *22*, 1485-1491.
17. Jansi Rani, B.; Dhivya, N.; Ravi, G.; Zance, S. S.; Yuvakkumar, R.; Hong, S. I. Electrochemical Performance of  $\beta$ -NiS@Ni(OH)<sub>2</sub> Nanocomposite for Water Splitting Applications. *ACS Omega* **2019**, *4*, 10302-10310.
  18. Zhang, C.; Higgins, T. M.; Park, S. H.; O'Brien, S. E.; Long, D.; Coleman, J. N.; Nicolosi, V. Highly Flexible and Transparent Solid-state Supercapacitors Based on RuO<sub>2</sub>/PEDOT:PSS Conductive Ultrathin Films. *Nano Energy* **2016**, *28*, 495-505.
  19. Urso, M.; Torrisi, G.; Boninelli, S.; Bongiorno, C.; Priolo, F.; Mirabella, S. Ni(OH)<sub>2</sub>@Ni Core-shell Nanochains as Low-cost High-rate Performance Electrode for Energy Storage Applications. *Sci. Rep.* **2019**, *9*, 7736.
  20. Park, H.-S.; Ko, S.-J.; Park, J.-S.; Kim, J.-Y. Song, H.-K. Redox-active Charge Carriers of Conducting Polymers as a Tuner of Conductivity and Its Potential Window. *Sci. Rep.* **2013**, *3*, 2454.
  21. Ovhal, M. M.; Kumar, N.; Hong, S.; Lee, H.; Kang, J.-W. Asymmetric Supercapacitor Featuring Carbon Nanotubes and Nickel Hydroxide Grown on Carbon Fabric: A Study of Self-discharging Characteristics. *J. Alloys Compd.* **2020**, *828*, 154447.
  22. Wang, W.; Guo, S.; Lee, I.; Ahmed, K.; Zhong, J.; Favors, Z.; Zaera, F.; Ozkan, M.; Ozkan, C.S. Hydrous Ruthenium Oxide Nanoparticles Anchored to Graphene and Carbon Nanotube Hybrid Foam for Supercapacitors. *Sci. Rep.* **2015**, *4*, 4452.
  23. Noori, A.; El-Kady, M. F.; Rahmanifar, M. S.; Kaner, R. B.; Mousavi, M. F. Towards Establishing Standard Performance Metrics for Batteries, Supercapacitors and Beyond. *Chem. Soc. Rev.* **2019**, *48*, 1272-1341.
  24. Chien, H. H.; Liao, C. Y.; Hao, Y. C.; Hsu, C. C.; Cheng, I. C.; Yu, I. S.; Chen, J. Z. Improved Performance of Polyaniline/Reduced-graphene-oxide Supercapacitor Using Atmospheric-pressure-plasma-jet Surface Treatment of Carbon Cloth. *Electrochim. Acta* **2018**, *260*, 391-399.
  25. Zhang, C.; Higgins, T. M.; Park, S. H.; O'Brien, S. E.; Long, D.; Coleman, J. N.; Nicolosi, V. Highly Flexible and Transparent Solid-state Supercapacitors Based on RuO<sub>2</sub>/PEDOT:PSS Conductive Ultrathin Films. *Nano Energy* **2016**, *28*, 495-505.
  26. Higgins, T. M.; Coleman, J. N. Avoiding Resistance Limitations in High-Performance Transparent Supercapacitor Electrodes Based on Large-Area, High-Conductivity PEDOT:PSS Films. *ACS Appl. Mater. Interfaces* **2015**, *7*, 16495-16506.

**Publisher's Note** The Polymer Society of Korea remains neutral with regard to jurisdictional claims in published articles and institutional affiliations.